Adaptive Control of Grid-Connected Inverters With Nonlinear LC Filters

Hossein Safamehr, Tooraj Abbasian Najafabadi, and Farzad Rajaei Salmasi, *Senior Member, IEEE*

***Abstract*—Distributed generation is an effective solution to clean, reliable, and cost-efficient energy supply. In this framework, inverters play a key role as energy converters. Accordingly, this article investigates the utilization of nonlinear inductive–capacitive (LC) filters for grid-connected inverters. Nonlinear LC filters are made of inductors with nonlinear B–H curves, which makes them have a smaller volume, less dissipation loss, and lower cost. The main drawback of using these filters, however, is their nonlinear current-dependent characteristics. To harness the undesirable impacts of nonlinear filters on the system performance, an adaptive observer-based control scheme is developed in this article. The proposed controller is based on a concurrent estimation of nonlinear inductor values, capacitor voltages, and grid-side currents. Based on its fast adaptation to plant changes, this scheme provides an improved stability margin and an inherent resonant damping characteristic under grid impedance uncertainty. Compared with the conventional approaches, this method requires no extra sensors. A comparative simulation and experimental analysis, based on a three-phase 7-kW inverter, is provided to validate the efficacy of the proposed control strategy.**

***Index Terms*—Adaptive observer, grid-connected inverter, Lyapunov function, nonlinear LC filter, PR control.**

I. Introduction

OVER the past decade or two, the use of renewable energy resources and distributed generations (DGs) has grown dramatically. This development provides the traditional energy systems with more market efficiency and grid reliability. As more and more DGs and microgrids appear, a more intelligent and interactive electrical system will be developed. The intelligent energy systems, comprising distributed energy resources, demand-response programming [1], and advanced inverters, help human societies with a clean and reliable energy future.

In microgrids, inverters play a crucial role. A grid-connected inverter converts the dc input of a local electrical power generator to an ac output with acceptable specifications based on the grid constraints [2]. Thus, the cost and performance of the inverters directly affect the operation of the microgrids.

Manuscript received 30 May 2022; revised 12 August 2022; accepted 13 September 2022. Date of publication 28 September 2022; date of current version 18 November 2022. Recommended for publication by Associate Editor F. W. Fuchs. *(Corresponding author: Hossein Safamehr.)*

Hossein Safamehr is with the Department of Electrical and Computer Engineering, Isfahan University of Technology, Isfahan 84156-83111, Iran (e-mail: h.safamehr@ec.iut.ac.ir).

Tooraj Abbasian Najafabadi and Farzad Rajaei Salmasi are with the Department of Electrical and Computer Engineering, University of Tehran, Tehran 1417935840, Iran (e-mail: najafabadi@ut.ac.ir; farzad_rs@ieee.org).

Color versions of one or more figures in this article are available at https://doi.org/10.1109/TPEL.2022.3209921.

Digital Object Identifier 10.1109/TPEL.2022.3209921

A grid-connected inverter is equipped with a low-pass filter in the output. Inductive (L), inductive–capacitive (LC), and inductive–capacitive–inductive (LCL) filters are commonly used in voltage-fed converters to attenuate the produced high-voltage harmonics at their outputs [3]. Although traditional L-type filters benefit from simplicity, they require a large inductor to suppress the harmonics. On the other hand, LC and LCL-type filters provide a higher harmonic attenuation. These filters, however, suffer from the potential resonance issue [4], [5]. Indeed, an LC-type filter is a second-order filter, but it acts like an LCL filter when connected to a grid inductance. It should also be noted that the resonance frequency of these LCL circuits varies by the variations of the grid impedance [6]. In general, grid impedance may vary due to power system configuration changes, transmission line maintenances, fault occurrence, etc.

Different active and passive damping methods have been proposed, in the literature, to suppress the resonance issue. Passive methods, such as a series resistor with the filter capacitor, benefits from simplicity. However, these methods suffer from problems such as power loss, lower attenuation, and increasing the number of elements [7]. Active damping methods, on the other hand, are based on the utilization of control frameworks, such as proportional-resonant (PR) control [8], optimal control [9], and robust control [10]. Adaptive control frameworks are also a group of active methods that use online grid impedance measurements to control the impacts of grid impedance variations [11], [12], [13].

The optimal design of LC and LCL filters is widely discussed in the literature. In the proposed algorithms, various design goals have been followed, including filter inductance ratio, resonance frequency [14], reactive power ratio, and current ripples [15], [16]. In these algorithms, cost factors are not generally considered, directly. In line with this issue, a precise look at filter elements can be beneficial. In LC and LCL filters, inductors impose high cost and space requirements. Generally, inductors are designed to operate linearly. As a consequence, a considerable capacity of the inductor cores remains unused. In other words, a significant reduction in size and cost of filters is achievable if the cores of the inductors are allowed to work in their nonlinear region of the B-H curve. By using this idea, nonlinear LC and LCL filters emerge.

Nonlinear inductors in power electronics circuits are investigated in several articles [17], [18], [19]. In these studies, the nonlinear behavior of the inductor is caused by reasons such as current and temperature variations. Likewise, the use of nonlinear inductors in grid-connected inverters is limited to a few works in recent years [2], [20], [21], [22]. In [20] a model predictive controller is presented to handle inductance variations due to

inductor current changes. This scheme benefits from offline calculations but loses optimality under large parameter variations. In [2], a combinational feedback framework is utilized to handle the effect of powder cores soft-saturation effect. This strategy is a transparent framework based on the weighted feedback of the inverter- and grid-side currents. The need for extra sensors and an accurate selection of feedback weights are the main challenges in this strategy. In [21], a model-based compensation method is proposed to handle nonlinear L-type filters. The impacts of grid impedance variations are not investigated in this study. Finally, the authors in [22] present a robust control scheme based on linear matrix inequalities where inductor nonlinearity and grid impedance variations are considered as system uncertainties. In this article, the resonant damping approach is not explicitly taken into account, while both nonlinear inductors and grid impedance variations exist.

In accordance with the discussed challenges, this article proposes an adaptive control scheme to handle the use of nonlinear LC filters in grid-connected inverters. The use of nonlinear filters entails serious impacts on both the total harmonic distortion (THD) of the inverter output current and the resonance frequency of the filter, which is exposed to grid impedance variations. In summary, this article provides as contribution a control scheme with three main features. First, the undesirable behavior of the nonlinear inductors is described by a time-varying model, and then, is compensated adaptively. Second, a concurrent estimation of the nonlinear inductor value, capacitor voltage, and grid-side current is provided by developing a Lyapunov-based observer. This observer eliminates the need for additional sensors to handle the existing nonlinearities. Finally, the proposed control scheme provides an inherent active resonance damping under grid impedance variations or weak grid connections. To validate the performance of the introduced scheme, both simulation and experimental results are provided.

In the sequence, Section II introduces the system modeling. Section III presents the control strategy and the challenges. In Section IV, the adaptive observer design procedure is provided. Section V presents the stability and robustness analysis of the control scheme. Section VI provides the experimental results validating the proposal. Finally, Section VII concludes this article.

II. System Modeling and Problem Formulation

In this section, the system modeling and the characteristics of nonlinear inductors are studied.

A. System Modeling

The system topology of a three-phase grid-connected inverter with a nonlinear LC filter is shown in Fig. 1. This topology comprises a three-phase inverter and a low-pass LC filter. The filter is connected to the grid through an isolating transformer. The combination of the LC filter and the inductances of the transformer and the grid acts as a resonant circuit. This LCL circuit may cause serious problems at its resonance frequency. By utilizing nonlinear inductors in the LC filters, the time-varying inductances of the filter and the grid make the resonance frequency shift over time.

In reality, the filter inductances are functions of the inverter-side currents. Therefore, they form a nonlinear model. In this

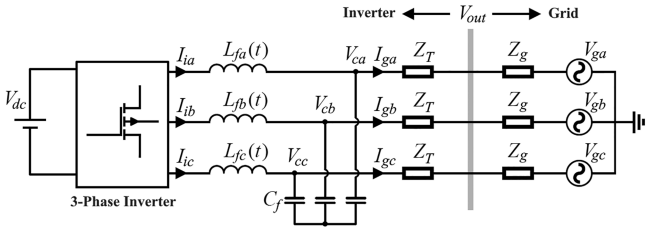

Fig. 1. Three-phase grid-connected inverter topology with nonlinear LC filter and time-varying grid inductances.

sense, the voltage–current equation of a nonlinear inductor is given by

$$v(t) = \left[L(i(t)) + \frac{dL(i(t))}{di} i(t)\right] \frac{di(t)}{dt} = L_e(t) \frac{di(t)}{dt} \quad (1)$$

where the nonlinear inductor is modeled by a time-varying effective inductance $L_e(t)$ [23]. The different values of inductances in each phase would introduce coupling between them. However, this coupling could be assumed small enough to be neglected [22]. Moreover, since there is no path for the zero-sequence currents, the system can be represented in the stationary reference frame by three single-phase systems.

Accordingly, the single-line state-space time-varying model of the inverter can be written as

$$\dot{x}(t) = A(t)x(t) + B(t)u(t)$$
$$y = Cx(t)$$

where :

$$x(t) = \begin{bmatrix} I_i \\ I_g \\ V_c \end{bmatrix}, \; A(t) = \begin{bmatrix} 0 & 0 & \frac{-1}{L_f(t)} \\ 0 & \frac{-R_p}{L_p} & \frac{1}{L_p} \\ \frac{1}{C_f} & \frac{-1}{C_f} & 0 \end{bmatrix}$$

$$B(t) = \begin{bmatrix} \frac{1}{L_f(t)} & 0 \\ 0 & \frac{-1}{L_p} \\ 0 & 0 \end{bmatrix}, u(t) = \begin{bmatrix} V_{\text{inv}}(t) \\ V_g(t) \end{bmatrix}, C = \begin{bmatrix} 0 \\ 1 \\ 0 \end{bmatrix}^T$$

$$R_p = R_T + R_g, \; L_p = L_T + L_g. \quad (2)$$

Here, V_{inv} is the inverter output voltage. V_g is the grid voltage. V_c, I_i, and I_g are the capacitor voltage, the inverter-side current, and the grid-side current, respectively. C_f and $L_f(t)$ are the capacitor and nonlinear inductor of the LC filter, respectively. $Z_T = R_T + j\omega L_T$ is the equivalent impedance of the isolating transformer, and $Z_g = R_g + j\omega L_g$ is the grid impedance where $\omega = 2\pi f$ is the angular frequency.

From the dynamical point of view, the values of both $L_f(t)$ and L_g change over time but with different rates of variation. While C_f is constant, the value of $L_f(t)$ changes by the instantaneous current flowing through the inductor winding. The L_g variation is, however, much slower, so it can be considered as an uncertain parameter.

So, the characteristic polynomial of the system (2) is

$$L_f(t)L_pC_fs^3 + L_f(t)C_fR_ps^2 + (L_f(t) + L_p)s + R_p = 0. \quad (3)$$

From (3), it can be noticed how time-varying parameters affect the resonance frequency of the system. The nominal plant parameters are presented in Table I. In the following, the nominal

TABLE I
NOMINAL SYSTEM PARAMETERS

Notation	Quantity	Value
P_n	Inverter nominal power	7 kW
E_n	Grid line to line voltage	380 V
f_g	Grid frequency	50 Hz
f_{sw}	Switching frequency	10.02 kHz
L_f/C_f	Filter inductance/capacitance	6.8 mH/5.5 μ F
L_T/R_T	Transformer inductance/resistance	1 mH/0.1 Ω
$L_{g,\text{nom}}$	Grid equivalent inductance	2 mH
$L_{g,\text{min}}$	Minimum grid inductance	0.5 mH
$L_{g,\text{max}}$	Maximum grid inductance	8 mH
R_g	Grid equivalent resistance	0.1 Ω

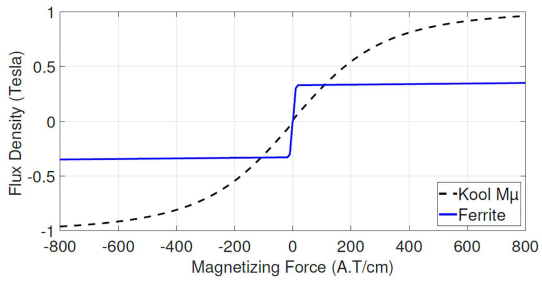

Fig. 2. Typical magnetization curves of Kool Mμ powder cores [25] and ferrite cores.

value of the grid impedance is represented by $L_{g,\text{nom}}$ and its variations are considered as $L_g \in [L_{g,\text{min}}, L_{g,\text{max}}]$.

B. Nonlinear Inductor

Powder cores are distributed air gap cores that are suitable for high-frequency applications. Compared with ferrite cores, powder ones have remarkable characteristics, such as higher saturation flux density, less sensitivity to temperature changes, and a softer saturation curve. The magnetization curves of a typical powder core and a ferrite core is compared in Fig. 2.

Generally, an inductor is designed such that it operates linearly. In a linear inductor, the core is not utilized by its whole capacity. So, bigger cores are required, which means higher cost, power dissipation, and space-occupancy. As a solution to this deficiency, the assumption of linearity could be relaxed. Accordingly, the inductors of the LC filter, listed in Table I, are designed for both linear and nonlinear cases. The related parameters are compared in Table II. In the linear design [24], the maximum flux density of the core is considered 0.44 T, whereas it is increased to 0.86 T in the nonlinear case. Increasing the maximum allowed flux density in the nonlinear inductor leads to 90% volume reduction. Moreover, the core loss density of Kool Mμ materials [25] is given by

$$P_{\text{loss}} = 52.36 \times V \times B^{1.988} f^{1.541} \tag{4}$$

TABLE II
INDUCTOR PARAMETERS

Parameter	Linear Inductor L_f	Nonlinear Inductor L_f
Inductor value	6.8 mH	6.8 mH
Core manufacturer	Magnetics	Magnetics
Core material	Kool Mμ	Kool Mμ
Core part number	0077102A7	0077908A7
Core cross section	358 mm^2	221 mm^2
Core volume	86,900 mm^3	43,400 mm^3
Number of stacks	5	1
Number of winding Turns	201	575
Maximum flux density	0.44 T	0.86 T
Core permeability variation on a current cycle	20 %	85 %

where V is the core volume, B is the core maximum flux density, and f is the core operating frequency. According to (4), a 90% reduction of the core volume and increasing the maximum flux density to 0.86 T lead to about 62% reduction in the power dissipation. In other words, the inductor cores are used more efficiently if their nonlinear behavior could be tolerated. Indeed, based on Fig. 2, the maximum decrease of powder core permeability is limited to 80% of the nominal value in the linear design [25]; while it may change down to 15% of the nominal value in the nonlinear case, during a working cycle. For more information, the detailed behavior of nonlinear inductors could be studied by using a time-variant current dependent model, based on the actual B-H magnetizing curve of the core [2].

III. CONTROL STRATEGY

As discussed, the proposed control scheme follows three main objectives that include the following:

1) compensating the impacts of the nonlinear inductors;
2) suppressing the resonance frequency in the presence of the nonlinear inductors and grid impedance variations;
3) using the minimum number of sensors, compared with the conventional frameworks.

In the conventional control strategies used for grid-connected inverters, one of the system states is commonly used as a feedback variable to regulate the output current. Each of these strategies has particular characteristics, which are studied in the literature [26]. To properly control the time-variant structure of the system (2), however, a combination of states may be required to be used as the feedback.

The main challenge in the control of the system (2) is handling the time-varying $L_f(t)$ and the uncertain Z_g. From the control standpoint, $L_f(t)$ has significant effects on both stability and performance of the system. The main effect of Z_g, however, is on the resonance frequency and the system stability. Accordingly, to meet the control goals of this article, one control signal candidate is

$$u_{\text{candidate}} = \alpha L_f(t) I_i + \beta L_f(t) I_g + (1 + \gamma L_f(t)) V_c \tag{5}$$

where α, β, and γ are control gains. $u_{\text{candidate}}$ forms a state-feedback control signal to cancel the variations of $L_f(t)$ and the impact of grid impedance variations on the system performance. Meanwhile, α, β, and γ control the characteristic polynomial of the system. By using this control signal, the modified system

matrix is derived from (2) and (5)

$$A_{\text{modified}}(t) = \begin{bmatrix} \alpha & \beta & \gamma \\ 0 & \frac{-R_p}{L_p} & \frac{1}{L_p} \\ \frac{1}{C_f} & \frac{-1}{C_f} & 0 \end{bmatrix}. \quad (6)$$

Hence, the characteristic polynomial of the system is

$\lambda(s) = s^3 + d_1\, s^2 + d_2 s + d_3$

where:

$$d_1 = \frac{R_p}{L_p} - \alpha,\ d_2 = \frac{1-\alpha R_p C_f - \gamma L_p}{L_p C_f},\ d_3 = \frac{\beta+\alpha+\gamma R_p}{L_p C_f}. \quad (7)$$

Referring (7), the control gains α, β, and γ should be tuned such that to ensure the following:

C1) the closed-loop stability against bounded changes of Z_g;
C2) proper resonance damping under bounded variations of Z_g;
C3) accurate tracking of sinusoidal references and compensating harmonics.

The proof of C1 and C2 can be derived from the Routh–Hurwitz stability criterion. This criterion must guarantee the system stability in all possible cases caused by uncertain (Z_g) or time-varying ($L_f(t)$) parameters. Property C3 can be ensured by utilizing a PR controller and harmonic compensators in the augmented system.

Based on the Routh–Hurwitz stability criterion, the control signal (5) is a stabilizing control input with a resonance damping property under bounded variations of the grid impedance, if and only if

$$\alpha < 0,\ \beta < 0 \text{ and } \gamma < 0. \quad (8)$$

There are still two more challenges to implement the discussed controlling idea. First, to implement (5), the instantaneous value of $L_f(t)$ is required because it is nonlinearly varying. Second, all system states should be measured to form $u_{\text{candidate}}$ that means requiring extra sensors. A solution to these problems is presented in the next section by developing a Lyapunov-based adaptive observer.

IV. Adaptive Observer

In the system (2), if all of the elements are assumed known, the overall system becomes observable. So, if the inverter-side current or the grid-side current is measured, the other one can be observed. In the studied problem, however, the grid impedance and the inductors of the LC filters are not constant or known. As mentioned earlier, the grid impedance dynamics are much slower than the controller dynamics. Moreover, the main effect of grid impedance is on the system stability, which is handled by the controller. So, if the controller and the observer dynamics are designed to be much faster than the grid impedance variations, then the constant assumption of grid impedance is still valid in the relatively fast time scale. The instantaneous value of the LC filter inductors, however, is constantly changing.

In the literature, a common approach for solving these kinds of problems is the quasi-static method. In this approach, the problem is cracked down into two parts. In each phase of the solving procedure, one of the parts is assumed constant, while the other is solved. The updated values are then used to solve the fixed part of the previous phase. This procedure is iterated until the parameters converge to the final values. This approach suffers from a significant computational effort. Moreover, it may converge to local minimums and cause errors.

In this article, a full-order Lyapunov-based observer is developed to provide smooth, fast, and jitterless estimations. The proposed observer is introduced in three steps, as follows.

A. Estimation Error Dynamics

By reforming (2) for the output voltage of the inverter setup, the estimated system can be defined as

$$\begin{aligned} \dot{\hat{I}}_i &= -\frac{1}{\hat{L}_f}\hat{V}_c + \frac{1}{\hat{L}_f}V_{\text{inv}} - f_i \\ \dot{\hat{I}}_g &= -\frac{R_T}{L_T}\hat{I}_g + \frac{1}{L_T}\hat{V}_c - \frac{1}{L_T}V_{\text{out}} - f_g \\ \dot{\hat{V}}_c &= \frac{1}{C_f}\hat{I}_i - \frac{1}{C_f}\hat{I}_g - f_c \end{aligned} \quad (9)$$

where the output voltage of the inverter setup is represented by V_{out}. Moreover, the estimated states and parameters are shown with the $\hat{}$ sign. By subtracting (9) from the actual system, the estimation error dynamics is driven as

$$\begin{aligned} \dot{\tilde{I}}_i &= -\frac{1}{L_f}V_c + \frac{1}{\hat{L}_f}\hat{V}_c + \frac{1}{\tilde{L}_f}V_{\text{inv}} + f_i \\ \dot{\tilde{I}}_g &= -\frac{R_T}{L_T}\tilde{I}_g + \frac{1}{L_T}\tilde{V}_c + f_g \\ \dot{\tilde{V}}_c &= \frac{1}{C_f}\tilde{I}_i - \frac{1}{C_f}\tilde{I}_g + f_c \end{aligned}$$

where

$$\begin{aligned} &\frac{1}{\tilde{L}_f} = \frac{1}{L_f} - \frac{1}{\hat{L}_f},\ \tilde{I}_i = I_i - \hat{I}_i,\ \tilde{I}_g = I_g - \hat{I}_g \\ &\tilde{V}_c = V_c - \hat{V}_c,\ f_i = K_i\tilde{I}_i,\ f_g = K_g\tilde{I}_i,\ f_c = K_c\tilde{I}_i \end{aligned} \quad (10)$$

where the estimation errors are shown with the $\tilde{}$ sign. f_i, f_g, and f_c represent observer correction functions with corresponding gains K_i, K_g, and K_c.

B. Adaption Laws

To eliminate the estimation error to zero, (10) can be rewritten as

$$\begin{bmatrix} \dot{\tilde{I}}_i \\ \dot{\tilde{I}}_g \\ \dot{\tilde{V}}_c \end{bmatrix} = \begin{bmatrix} K_i & 0 & -\frac{1}{L_f} \\ K_g & -\frac{R_T}{L_T} & \frac{1}{L_T} \\ \frac{1}{C_f} + K_c & -\frac{1}{C_f} & 0 \end{bmatrix} \begin{bmatrix} \tilde{I}_i \\ \tilde{I}_g \\ \tilde{V}_c \end{bmatrix} + \begin{bmatrix} V_{\text{inv}} - \hat{V}_c \\ 0 \\ 0 \end{bmatrix} \begin{bmatrix} \frac{1}{\tilde{L}_f} \end{bmatrix} \quad (11)$$

in which the estimation error dynamics are described in terms of $\dot{\tilde{X}} = A\tilde{X} + \omega^T\tilde{\theta}$. In (11), the estimation errors of states and parameters are separated by $\tilde{X}$ and $\tilde{\theta}$.

Consequently, to develop the adaptation laws of the estimator, the following Lyapunov function is proposed:

$$V = \tilde{X}^T\tilde{X} + \tilde{\theta} = \tilde{I}_i^2 + \tilde{I}_g^2 + \tilde{V}_c^2 + \eta\tilde{L}_1^2 \geq 0 \quad (12)$$

where η is a positive constant. The time derivative of (12) is given by

$$\dot{V} = 2\tilde{I}_i\dot{\tilde{I}}_i + 2\tilde{I}_g\dot{\tilde{I}}_g + 2\tilde{V}_c\dot{\tilde{V}}_c + 2\eta\tilde{L}_1\dot{\tilde{L}}_1. \tag{13}$$

The Lyapunov-candidate-function V is globally positive definite, so the system equilibrium, which is zero, is proven to be globally asymptotically stable, if and only if the time derivative of the Lyapunov-candidate-function is globally negative definite. Based on this, adaption laws can be derived.

By substituting (10) into (13), and after some calculation, the $\dot{V}$ can be separated into three subfunctions $\dot{V}_1$, $\dot{V}_2$, and $\dot{V}_3$ given by

$$\begin{aligned}\dot{V} = &\left[-\tilde{I}_i\frac{1}{L_f}\tilde{V}_c + (\tilde{I}_i)(-\hat{V}_c + V_{\text{inv}})\left(\frac{1}{\tilde{L}_f}\right) + \tilde{I}_g K_g \tilde{I}_i\right.\\ &\left. + \tilde{I}_g\frac{\tilde{V}_c}{L_T} + \tilde{V}_c\left(\frac{1}{C_f} + K_c\right)\tilde{I}_i - \tilde{V}_c\frac{\tilde{I}_g}{C_f} - \frac{R_T}{L_T}\tilde{I}_g^2\right]\\ &+ [K_i\tilde{I}_i^2] + [\eta\tilde{L}_f\dot{\tilde{L}}_f] = \dot{V}_1 + \dot{V}_2 + \dot{V}_3. \end{aligned}\tag{14}$$

The first part $\dot{V}_1$ can be rewritten in the quadratic form as

$$\dot{V}_1 = \tilde{X}^T\Omega\tilde{X}$$

where

$$\tilde{X}^T = \begin{bmatrix}\tilde{I}_i & \tilde{I}_g & \tilde{V}_c & \frac{1}{\tilde{L}_f}\end{bmatrix}$$

$$\Omega = \begin{bmatrix} 0 & 0 & \frac{-1}{L_f} & -\hat{V}_c + V_{\text{inv}} \\ K_g & -\frac{R_T}{L_T} & \frac{1}{L_T} & 0 \\ \frac{1}{C_f} + K_c & -\frac{1}{C_f} & 0 & 0 \\ 0 & 0 & 0 & 0 \end{bmatrix}. \tag{15}$$

Based on the eigenvalues of Ω, it is concluded that there exists some K_c and K_g that make the Ω negative semidefinite, and subsequently, $\dot{V}_1 \leq 0$.

The second term of $\dot{V}$ yields as $\dot{V}_2 = K_i\tilde{I}_i^2$. It is straightforward to show that the estimation error of a parameter is not zero. So, $\dot{V}_2$ can have a desirably large negative value by tuning K_i.

Finally, $\dot{V}$ is negative if $\dot{V}_3$ is negative or positively bounded because the proper selection of K_i will result in an overall negative summation. $\dot{V}_3$ defines the inductor estimation equations, which is studied in the next section.

C. Inductor Estimation

The third term of $\dot{V}$ is given by $\dot{V}_3 = [\eta\tilde{L}_f\dot{\tilde{L}}_f]$. Let define the model of the inductor and the estimator as $Z = \theta u$ and $\hat{Z} = \hat{\theta}u$, respectively. Here, θ is the unknown parameter, Z is the output, and u is the input. In this case, the estimation error can be defined as

$$\varepsilon = \frac{Z - \hat{Z}}{m_s^2} \tag{16}$$

in which $m_s^2 = 1 + \Gamma u^2$ is the normalizing factor, and Γ is a positive constant. $\hat{\theta}$ can be computed by using the following cost function to minimize the error:

$$J(\hat{\theta}) = \frac{\varepsilon^2 m_s^2}{2} = \frac{(Z - \hat{\theta}u)^2}{2m_s^2}. \tag{17}$$

By using a gradient-based method, $\dot{\hat{\theta}}$ is derived as

$$\dot{\hat{\theta}} = \rho\varepsilon u \tag{18}$$

where ρ is the adaption gain, which is a positive constant. The stability and convergence of (18) can be examined by defining the estimation error as $\text{err} = \theta - \hat{\theta}$ and solving the differential equation of err.

By returning to the inductor estimation problem, the describing equation of L_f is given by

$$sL_fI_i = V_{\text{inv}} - V_c. \tag{19}$$

So

$$\theta = L_f, \quad Z = \frac{V_{\text{inv}} - V_c}{s + \psi}, \quad u = \frac{sI_i}{s + \psi} \tag{20}$$

where the input and output functions are divided by $s + \psi$ to make them regular. Also, ψ provides a degree of freedom in the design procedure. Thus, the estimated value of L_f can be expressed as

$$\dot{\hat{L}}_f = \rho\left(\frac{V_{\text{inv}} - \hat{V}_c - \hat{L}_f\hat{I}_i s}{{m_s}^2(s + \psi)}\right)\left(\frac{s\hat{I}_i}{s + \psi}\right). \tag{21}$$

Therefore, $\dot{V}$ is negative definite, if K_i, K_g, and K_c are properly tuned, and (21) is initiated with a limited value to guarantee $\dot{V}_3$ to be bounded.

All in all, the adaptive observer equations can be defined as

$$\begin{aligned}\dot{\hat{I}}_i &= -\frac{1}{\hat{L}_f}\hat{V}_c + \frac{1}{\hat{L}_f}V_{\text{inv}} - K_i\tilde{I}_i\\ \dot{\hat{I}}_g &= -\frac{R_T}{L_T}\hat{I}_g + \frac{1}{L_T}\hat{V}_c - \frac{1}{L_T}V_{\text{out}} - K_g\tilde{I}_i\\ \dot{\hat{V}}_c &= \frac{1}{C_f}\hat{I}_i - \frac{1}{C_f}\hat{I}_g - K_c\tilde{I}_i\\ \dot{\hat{L}}_1 &= \rho\left(\frac{V_{\text{inv}} - \hat{V}_c - \hat{L}_f\hat{I}_i s}{{m_s}^2(s + \psi)}\right)\left(\frac{s\hat{I}_i}{s + \psi}\right).\end{aligned}\tag{22}$$

So, (22) provides an estimation of $L_f(t)$, $V_c(t)$, and $I_g(t)$ from the measurements of $I_i(t)$ and $V_{\text{out}}(t)$.

V. Stability and Robustness Analysis

In this section, the stability and robustness of the proposed control scheme are investigated. Here, L_g is considered as an uncertain parameter. This perspective reveals how different values of the grid impedance may affect the stability of the closed-loop system. This analysis is based on the model parameters listed in Tables I and II. The control parameters are also shown in Table III. The overall control scheme block diagram is shown in Fig. 3. G_c represents the control block, defined by (5), where the control gains are tuned based on the root locus controller design method. G_{PR} block represents a PR controller. The PR controller improves the sinusoidal reference tracking by applying high gains at the desired frequencies. This controller is expressed as

$$G_{\text{PR}}(s) = K_p + \frac{K_1\omega_c s}{s^2 + 2\omega_c s + \omega_r^2} \tag{23}$$

where $\omega_r = 2\pi f_{\text{res}}$ defines the resonant frequency. K_p is the proportional gain, K_1 is the resonant gain at ω_r, and $\omega_c = 2\pi f_c$ defines the cutoff frequency.

TABLE III
CONTROL SYSTEM PARAMETERS

Notation	Quantity	Value
$\alpha,\ \beta,\ \gamma$	Control gains	-600, -1, -600
$K_i,\ K_g,\ K_c$	Adaptation gains	-170, 7.7×10^{-8}, 4.7×10^{6}
$\eta,\ \Gamma,\ \rho,\ \psi$	Inductor estimation gains	1, 1, 50000, 0.01
K_p	Proportional gain	165
K_1	Gain of first resonant gain	170
ω_c	Cutoff frequency (PR)	15 rd/s

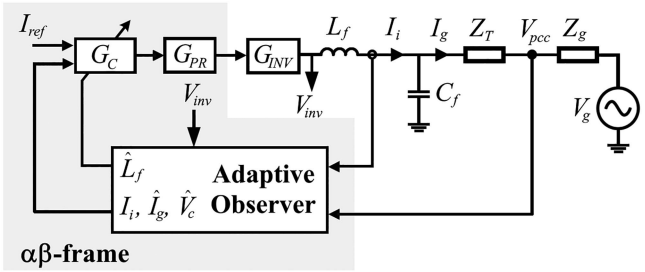

Fig. 3. Control scheme block diagram.

The system root loci of the discrete control scheme is shown in Fig. 4(a). To clearly show the possible resonances of the LCL circuit, the $G_{\rm PR}$ block is considered as a gain block in this analysis. The poles and zeros of the closed-loop system are specified with crosses and circles, respectively. It can be noticed from the root locus diagram that the system is stable for all $k > 0$. Moreover, by applying the proposed control scheme, the resonance frequency of the LCL circuit is actively damped. In this analysis, one sample delay is considered to model the delay of the digital processing.

Generally, an uncertain transfer function $h(s)$ can be constructed [27] as

$$h(s) = h_0(s) + \delta(s), \quad \delta(s) \in d \tag{24}$$

where $h_0(s)$ is the nominal transfer function, and d is the set of all allowed perturbations. As discussed earlier, the grid impedance variation is the main set of uncertainties in the grid-connected inverters. Accordingly, Fig. 4(b) shows a sweep in the closed-loop eigenvalues, while L_g changes from 25% ($L_{g,\rm min}$) to 400% ($L_{g,\rm max}$) of its measured value ($L_{g,\rm nom}$).

It is observed from Fig. 4(b) that there are no instability or resonance issues caused by the uncertain parameter L_g. Moreover, the studied uncertainties do not have a significant effect on the closed-loop gain margin and phase margin. So, the proposed control scheme provides a robust structure against grid impedance variations.

VI. EXPERIMENTAL RESULTS

In this section, the experimental tests on a three-phase 7-kW inverter are carried out to investigate the performance of the proposed control structure. The system and control parameters are listed in Tables I–III. A 32-bit floating-point TMS320F28335 DSP is used to implement the controller. Voltage and current

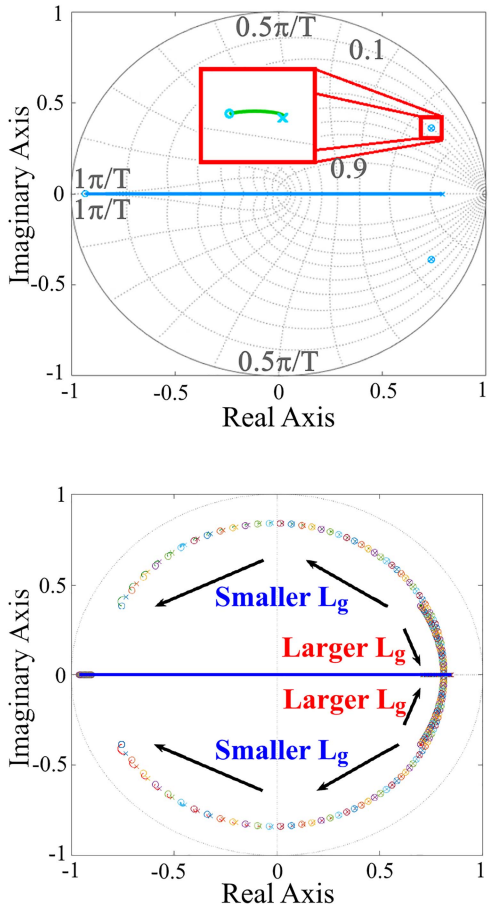

Fig. 4. (a) System root locus diagram. (b) Closed-loop eigenvalues of the system when L_g varies between 25% to 400% of the measured value.

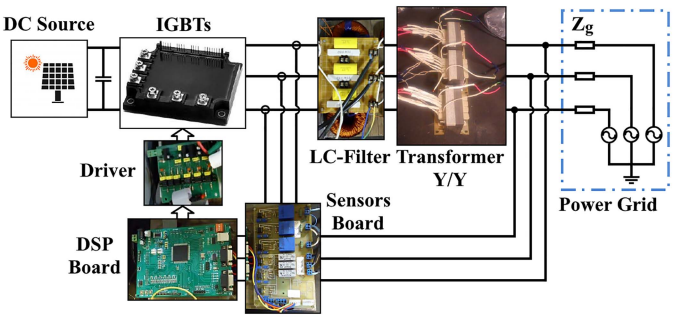

Fig. 5. Experimental setup configuration.

waveforms are measured by a 12-bit resolution analog-to-digital converter. The switching dead time of the IGBT modules is considered 3 μs. The experimental setup configuration is shown in Fig. 5. In the following analysis, the controllers are designed for the optimum operating point of the inverter, which is considered 90% of the rated power.

Fig. 6 shows the performance of the adaptive observer on estimating the instantaneous values of the nonlinear inductor, capacitor voltage, and grid-side current, respectively. As the results show, the observer outputs have converged to the actual values after a short time.

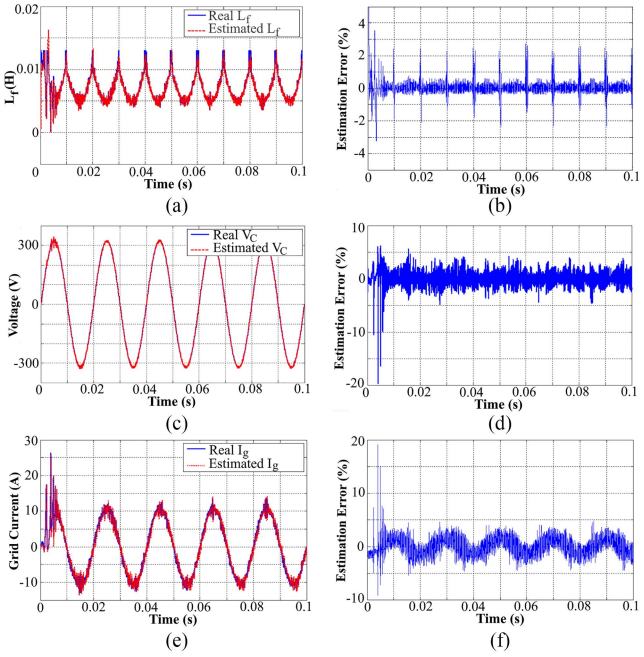

Fig. 6. Actual and estimated values, and estimation error of the (a),(b) nonlinear inductor, (c),(d) capacitor voltage, and (e),(f) grid-side current. (a) Estimation of L_f. (b) Estimation error of L_f. (c) Estimation of V_c. (d) Estimation error of V_c. (e) Estimation of I_g. (f) Estimation error of I_g.

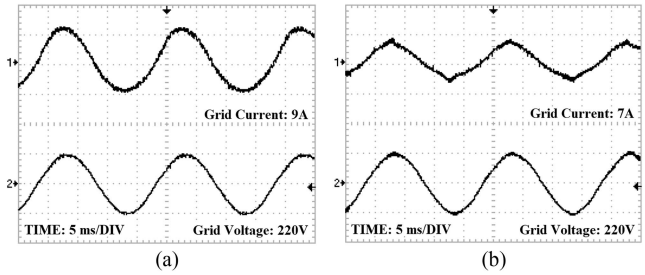

Fig. 7. Grid currents with the conventional PR control in the presence of (a) linear inductors (THD = 1.9%) and (b) nonlinear inductors (THD = 5.4%).

In the first scenario, the impact of nonlinear inductors on the PR control systems is studied. In this test, the control design is conducted based on the conventional linear model of the LC filters. Fig. 7 depicts that the THD and steady-state error of the grid current increase when linear inductors are replaced by nonlinear ones. In addition, no guarantee of stability is provided in this scenario when the operating point changes.

In the next scenario, the performance of the proposed adaptive controller is evaluated under nonlinear inductors and weak grid conditions. In this test, the control gains are selected based on $L_{g,\text{nom}} = 2$ mH. To evaluate the effect of grid impedance variations on the closed-loop system, Fig. 8(a)–(d) depicts the grid voltage and current under $L_g = 0.5$ mH, $L_g = 2$ mH, $L_g = 4$ mH, and $L_g = 8$ mH, respectively. The results show the low sensitivity of the closed-loop response to grid impedance variations.

In the next test, the performance of the proposed scheme is investigated in the presence of both grid impedance variations and

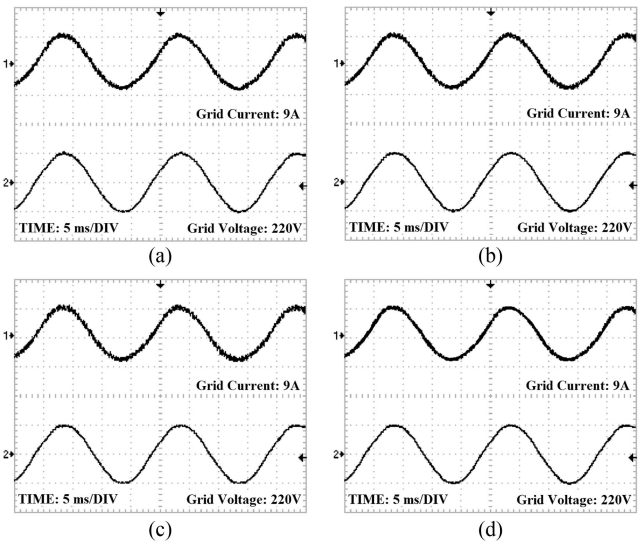

Fig. 8. Grid current and voltage with adaptive control in the presence of nonlinear inductors and under (a) $L_g = 0.5$ mH (THD = 1.9%), (b) $L_g = 2$ mH (THD = 2.4%), (c) $L_g = 4$ mH (THD = 2.6%), and (d) $L_g = 8$ mH (THD = 2.8%).

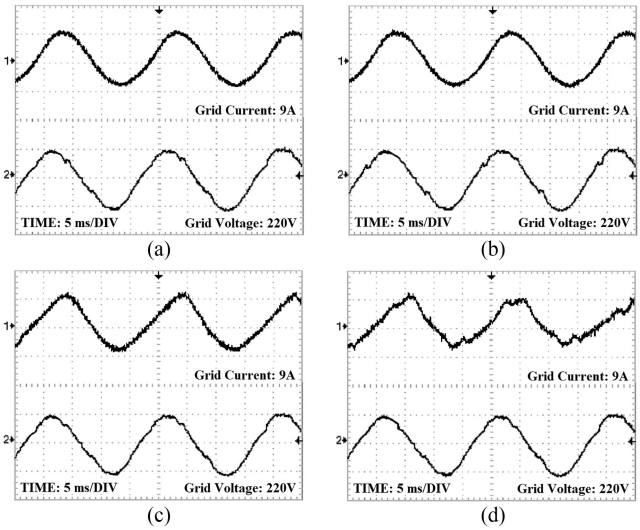

Fig. 9. Grid current and voltage with adaptive control under nonlinear inductors and distorted grid voltages with (a) $L_g = 0.5$ mH (THD = 2.2%), (b) $L_g = 2$ mH (THD = 2.7%), (c) $L_g = 4$ mH (THD = 4.6%), and (d) $L_g = 8$ mH (THD = 8.6%).

distorted grid voltages. Here, the distorted voltage is considered in accordance with the upper limits of the Standard EN50160. Based on this Standard, the maximum values of the third, fifth, and seventh harmonic components of the grid voltage are not allowed to exceed 5%, 6%, and 5%, respectively [28]. Accordingly, Fig. 9 shows the performance of the control system in mitigating the effect of the harmonics under previous conditions. In Fig. 9, it can be observed that the grid current complies with the grid requirements under grid impedance variations between 25% and 200% of the nominal value. For $L_g = 8$ mH (400% of the nominal value), however, the THD is more than 5%. Although the THD requirement is not satisfied in this condition,

TABLE IV
CONTROLLER PERFORMANCE UNDER GRID IMPEDANCE VARIATIONS

Parameter	25% of Nominal	Nominal	200% of Nominal
Transient duration	$\leq$ 40 ms	$\leq$ 40 ms	$\leq$ 40 ms
Over/under shoot	1.5 %	1.4 %	0.88 %
Transient THD	6.1 %	5.5 %	5.9%
Steady-State THD	1.9 %	2.4 %	2.9%
Steady-State Error	1.5 %	1 %	2 %

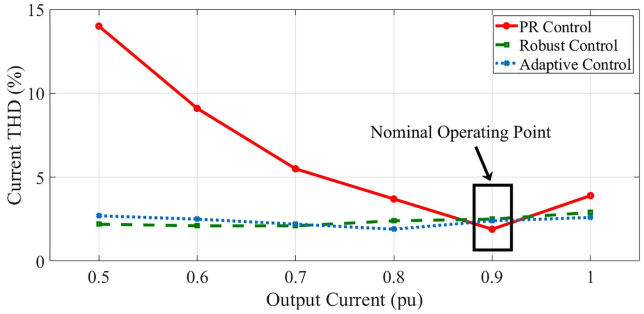

Fig. 10. Impacts of output current variations on the performance of the PR and adaptive control schemes in the presence of nonlinear inductors.

it can be seen that the system stability is preserved, and the resonances are damped.

Table IV provides an analysis of the dynamic and steady-state performance of the proposed strategy. In this analysis, the grid impedance changes from 25% to 200% of its nominal value. In all cases, a unit step reference signal is applied to the closed-loop system to increase the inverter output current from 0 to 0.9 p.u. The results depict that the controller has effectively handled the grid impedance variations during transient and steady-state phases.

To perform a comparative analysis, the performances of the conventional PR control, the linear-matrix-inequalities-based robust control presented in [22], and the proposed adaptive scheme are investigated in Fig. 10. In all schemes, the control gains are tuned for the optimum operating point in the presence of nonlinear inductors. The PR controller uses the fundamental, fifth-, and seventh-order harmonic compensators, which are tuned to 140, 20, and 25, respectively. The gain vector of the robust controller is selected as

$$K = [-15.043 \ -1.880 \ -10.879 \ -0.734 \ 30.101 \ -30.639 \ 30.274 \ -25.493 \ 20.664 \ -40.105 \ 30.444 \ -50.091]. \quad (25)$$

It is validated from Fig. 10 that the robust and the proposed adaptive scheme satisfy the IEEE-1547 Standards (THD$\leq$5%) [29]. Moreover, these schemes show a consistent performance under output current variations, while the performance of the PR control significantly degrades by moving away from the designed operating point. In this scenario, the system response may become unstable under PR control [22].

Finally, Table V provides a parametric comparison between the discussed control systems with nonlinear inductors. In summary, the PR control benefits from simplicity but it cannot guarantee the system robustness against voltage distortions or grid impedance variations. On the contrary, the robust scheme provides good robustness against system uncertainties. Among all strategies, however, the adaptive scheme presents better harmonic cancellation because of its inherent adaptation characteristics. Computation burden and design complexity are two other parameters compared in Table V. The results show a tradeoff between cost and performance. The PR control imposes a lower computational burden and complexity but leads to lower performance, too. On the other hand, the robust and adaptive schemes need more computational resources but provide a more reliable structure in the presence of nonlinear inductors.

TABLE V
COMPARISON BETWEEN DIFFERENT CONTROL SCHEMES IN THE PRESENCE OF NONLINEAR INDUCTORS

Scenario	Parameter	PR control	Robust control [22]	Adaptive control
Grid	THD ($L_{g,\min}$)	1.8 %	2.1 %	1.9 %
Impedance	THD ($L_{g,\text{nom}}$)	2.1 %	2.9 %	2.4 %
Variations	THD ($L_{g,\max}$)	15.4 %	3.3 %	2.8 %
Transient	THD ($L_{g,\min}$)	$\leq$ 40 ms	$\leq$ 40 ms	$\leq$ 40 ms
Phase	THD ($L_{g,\text{nom}}$)	$\leq$ 40 ms	$\leq$ 40 ms	$\leq$ 40 ms
Duration	THD ($L_{g,\max}$)	$\leq$ 60 ms	$\leq$ 40 ms	$\leq$ 60 ms
Steady-	THD ($L_{g,\min}$)	1 %	2.4 %	1.7 %
State	THD ($L_{g,\text{nom}}$)	1 %	2.4 %	1 %
Error	THD ($L_{g,\max}$)	2.5 %	4.1 %	2.1 %
Grid with	THD ($L_{g,\min}$)	6.6 %	2.0 %	2.2 %
Distorted	THD ($L_{g,\text{nom}}$)	10.1 %	3.1 %	2.7 %
Voltage	THD ($L_{g,\max}$)	24.9 %	4.6 %	8.6 %
Operating point	Minimum THD	1.8 %	2.1 %	1.9 %
Variation	Maximum THD	14.1 %	2.9 %	2.4 %
Computational burden		3 μs	8 μs	9 μs
Design complexity (No. of control gains)		5	12	12

VII. CONCLUSION

In grid-connected inverters, designing the inductors to operate in their nonlinear flux-current region yields a reduction in cost, inductor size, and power loss. The main drawback of these inductors, however, is their time-varying, nonlinear behavior. To harness its undesirable impacts on the system performance, an adaptive observer-based control scheme is developed in this article. The proposed controller is based on a concurrent estimation of the nonlinear inductors, capacitor voltages, and grid-side currents. The proposed observer eliminates the necessity of using extra sensors. The stability of the proposed observer is proved analytically based on the Lyapunov theory. The proposed control scheme guarantees system stability and resonance damping under grid impedance variations. A robust stability analysis is performed to certify these characteristics. Finally, an experimental setup, including a three-phase 7-kW inverter system, was used to provide a comparative analysis among the conventional PR control, a robust strategy, and the proposed adaptive method.

REFERENCES

[1] H. Safamehr and A. Rahimi-Kian, "A cost-efficient and reliable energy management of a micro-grid using intelligent demand-response program," *Energy*, vol. 91, pp. 283–293, 2015.

[2] H. Safamehr, T. A. Najafabadi, and F. R. Salmasi, "Enhanced control of grid-connected inverters with non-linear inductor in LCL filter," *IET Power Electron.*, vol. 9, no. 10, pp. 2111–2120, 2016.

[3] U. P. Yagnik and M. D. Solanki, "Comparison of L, LC & LCL filter for grid connected converter," in *Proc. IEEE Int. Conf. Trends Electron. Inform.*, 2017, pp. 455–458.

[4] S. Jiang and Y. Liu, "EMI noise reduction for the single-phase grid-connected inverter with a modified harmonic filter design," *IEEE Trans. Electromagn. Compat.*, vol. 63, no. 3, pp. 739–751, Jun. 2021.

[5] P. Evald, R. V. Tambara, and H. A. Gründling, "A direct discrete-time reduced order robust model reference adaptive control for grid-tied power converters with LCL filter," *Revista Eletrônica de Potência*, vol. 25, no. 3, pp. 361–372, 2020.

[6] N. Rasekh and M. Hosseinpour, "LCL filter design and robust converter side current feedback control for grid-connected proton exchange membrane fuel cell system," *Int. J. Hydrogen Energy*, vol. 45, no. 23, pp. 13055–13067, 2020.

[7] R. Pena-Alzola, M. Liserre, F. Blaabjerg, R. Sebastián, J. Dannehl, and F. W. Fuchs, "Analysis of the passive damping losses in LCL-filter-based grid converters," *IEEE Trans. Power Electron.*, vol. 28, no. 6, pp. 2642–2646, Jun. 2013.

[8] G. Shen, X. Zhu, J. Zhang, and D. Xu, "A new feedback method for PR current control of LCL-filter-based grid-connected inverter," *IEEE Trans. Ind. Electron.*, vol. 57, no. 6, pp. 2033–2041, Jun. 2010.

[9] S. A. Khajehoddin, M. Karimi-Ghartemani, and M. Ebrahimi, "Optimal and systematic design of current controller for grid-connected inverters," *IEEE Trans. Emerg. Sel. Topics Power Electron.*, vol. 6, no. 2, pp. 812–824, Jun. 2017.

[10] R. Guzman, L. G. de Vicuna, J. Morales, M. Castilla, and J. Miret, "Model-based active damping control for three-phase voltage source inverters with LCL filter," *IEEE Trans. Power Electron.*, vol. 32, no. 7, pp. 5637–5650, Jul. 2017.

[11] T. Roinila, M. Vilkko, and J. Sun, "Online grid impedance measurement using discrete-interval binary sequence injection," *IEEE Trans. Emerg. Sel. Topics Power Electron.*, vol. 2, no. 4, pp. 985–993, Dec. 2014.

[12] R. Luhtala, T. Messo, T. Reinikka, J. Sihvo, T. Roinila, and M. Vilkko, "Adaptive control of grid-connected inverters based on real-time measurements of grid impedance: DQ-domain approach," in *Proc. IEEE Energy Convers. Congr. Expo.*, 2017, pp. 69–75.

[13] L. Jessen and F. W. Fuchs, "Modeling of inverter output impedance for stability analysis in combination with measured grid impedances," in *Proc. IEEE 6th Int. Symp. Power Electron. Distrib. Gener. Syst.*, 2015, pp. 1–7.

[14] P. Channegowda and V. John, "Filter optimization for grid interactive voltage source inverters," *IEEE Trans. Ind. Electron.*, vol. 57, no. 12, pp. 4106–4114, Dec. 2010.

[15] A. Kouchaki and M. Nymand, "Analytical design of passive LCL filter for three-phase two-level power factor correction rectifiers," *IEEE Trans. Power Electron.*, vol. 33, no. 4, pp. 3012–3022, Apr. 2018.

[16] Y. Tang, W. Yao, P. C. Loh, and F. Blaabjerg, "Design of LCL filters with LCL resonance frequencies beyond the Nyquist frequency for grid-connected converters," *IEEE Trans. Emerg. Sel. Topics Power Electron.*, vol. 4, no. 1, pp. 3–14, Mar. 2016.

[17] W. Yuan, Y. Wang, D. Liu, F. Deng, and Z. Chen, "Parameter estimator-based power control strategy of microgrid considering nonlinear inductor," in *Proc. IEEE Appl. Power Electron. Conf. Expo.*, 2021, pp. 83–88.

[18] H. Cha and T.-K. Vu, "Comparative analysis of low-pass output filter for single-phase grid-connected photovoltaic inverter," in *Proc. 25th Annu. IEEE Appl. Power Electron. Conf. Expo.*, 2010, pp. 1659–1665.

[19] R. A. Mastromauro, M. Liserre, and A. Dell'Aquila, "Study of the effects of inductor nonlinear behavior on the performance of current controllers for single-phase PV grid converters," *IEEE Trans. Ind. Electron.*, vol. 55, no. 5, pp. 2043–2052, May 2008.

[20] T.-F. Wu, K.-H. Sun, C.-L. Kuo, and C.-H. Chang, "Predictive current controlled 5-kW single-phase bidirectional inverter with wide inductance variation for DC-microgrid applications," *IEEE Trans. Power Electron.*, vol. 25, no. 12, pp. 3076–3084, Dec. 2010.

[21] Q. Wei, B. Liu, and S. Duan, "Current ripple analysis and controller design for grid-connected converters considering the soft-saturation nature of the powder cores," *IEEE Trans. Power Electron.*, vol. 33, no. 10, pp. 8827–8837, Oct. 2018.

[22] C. R. D. Osório, G. G. Koch, H. Pinheiro, R. C. Oliveira, and V. F. Montagner, "Robust current control of grid-tied inverters affected by LCL filter soft-saturation," *IEEE Trans. Ind. Electron.*, vol. 67, no. 8, pp. 6550–6561, Aug. 2020.

[23] W. H. Wolfle and W. G. Hurley, "Quasi-active power factor correction with a variable inductive filter: Theory, design and practice," *IEEE Trans. Power Electron.*, vol. 18, no. 1, pp. 248–255, Jan. 2003.

[24] Magnetics, "Magnetics inductor design tool." Accessed: Sep. 2022. [Online]. Available: https://www.mag-inc.com/Design/Design-Tools/Inductor-Design

[25] Magnetics, "$kool m\mu$ material curves." Accessed: Sep. 2022. [Online]. Available: https://www.mag-inccom/Products/Powder-Cores/Kool-Mu-Cores/Kool-Mu-Material-Curves

[26] Q. Liu, T. Caldognetto, and S. Buso, "Review and comparison of grid-tied inverter controllers in microgrids," *IEEE Trans. Power Electron.*, vol. 35, no. 7, pp. 7624–7639, Jul. 2020.

[27] S. Skogestad and I. Postlethwaite, *Multivariable Feedback Control: Analysis and Design*, vol. 2. Wiley, 2007.

[28] "Guide, Power Quality Application, "Voltage disturbances"," Standard EN 50160, 2004.

[29] T. S. Basso and R. DeBlasio, "IEEE 1547 series of standards: Interconnection issues," *IEEE Trans. Power Electron.*, vol. 19, no. 5, pp. 1159–1162, Sep. 2004.

Hossein Safamehr received the B.Sc. degree in electrical engineering from the University of Isfahan, Isfahan, Iran, in 2012, the M.Sc. degree in electrical engineering from the University of Tehran, Tehran, Iran, in 2015. He is currently working toward the Ph.D. degree in control of grid-forming inverters with the Isfahan University of Technology, Isfahan.

His main research interests include power systems control, industrial control systems, power electronics, and smart energy networks.

Tooraj Abbasian Najafabadi received the B.S. degree in electrical engineering from the Isfahan University of Technology, Isfahan, Iran, in 2003, and the M.S. and Ph.D. degrees in electrical engineering from the University of Tehran, Tehran, Iran, in 2005 and 2009, respectively.

He is currently an Assistant Professor with the School of Electrical and Computer Engineering, University of Tehran. His main research interests include nonlinear and adaptive control, design and control of advanced motor drives, power electronic systems, hybrid electric vehicles, and mechatronics.

Farzad Rajaei Salmasi (Senior Member, IEEE) received the B.S. degree in electrical engineering from the Sharif University of Technology, Tehran, Iran, in 1994, the M.Sc. degree in electrical engineering from the Amirkabir University of Technology, Tehran, in 1997, and the Ph.D. degree in electrical engineering from Texas A&M University, College Station, TX, USA, in 2002.

From 1999 to 2002, he was a Research Assistant with the Advanced Motor Drives and Hybrid Vehicles Laboratory, Department of Electrical Engineering, Texas A&M University. From 2002 to 2004, he was a Research Scientist with Electro Standards Laboratories, Cranston, RI, USA. In 2004, he joined the School of Electrical and Computer Engineering, Faculty of Engineering, University of Tehran. He started visiting the University of Toronto in 2015. His main research interests include design and control of advanced electric motor drives, power electronic systems, hybrid electric vehicles, microgrids, and smart grids.

Dr. Salmasi is an Associate Editor for the IEEE TRANSACTIONS ON INDUSTRIAL ELECTRONICS.